

Pulsing corals: A story of scale and mixing

Julia E. Samson¹, Nicholas A. Battista², Shilpa Khatri³, Laura A. Miller^{1,4}

¹Dept. of Biology, ⁴Dept. of Mathematics

University of North Carolina at Chapel Hill, Chapel Hill, NC, USA

jesamson@live.unc.edu, lam9@unc.edu

² Dept. of Mathematics and Statistics

The College of New Jersey, Ewing, NJ, USA

battistn@tcnj.edu

³Applied Mathematics Unit, School of Natural Sciences

University of California Merced, Merced, CA, USA

skhatri3@ucmerced.edu

Received: 14 September 2017, accepted: 16 December 2017, published: 27 December 2017

Abstract—Effective methods of fluid transport vary across scale. A commonly used dimensionless number for quantifying the effective scale of fluid transport is the frequency based Reynolds number, Re_f , which gives the ratio of inertial to viscous forces in a fluid flow. What may work well for one Re_f regime may not produce significant flows for another. These differences in scale have implications for many organisms, ranging from the mechanics of how organisms move through their fluid environment to how hearts pump at various stages in development. Some organisms, such as soft pulsing corals, actively contract their tentacles to generate mixing currents that enhance photosynthesis. Their unique morphology and the intermediate Re_f regime at which they function, where both viscous and inertial forces are significant, make them a unique model organism for understanding fluid mixing. In this paper, 3D fluid-structure interaction simulations of a pulsing soft coral are used to quantify fluid transport and describe fluid mixing across a wide range of Re_f . The results show that net transport is negligible

for $Re_f < \mathcal{O}(10^1)$, and continuous upward flow is produced for $Re_f \geq \mathcal{O}(10^1)$. Sustained net transport is necessary to bring in new fluid for sampling and to remove waste. As the Re is increased well above $\mathcal{O}(10^1)$, the slow region of mixing necessary for gas exchange between the tentacles is reduced. Since corals live at Re_f between about 8 and 36, the flows they produce are defined by sustained net transport of fluid away from the coral in a continuous upward jet and a slow region of mixing between the tentacles necessary for gas exchange.

Keywords—pulsing coral; coral reefs; immersed boundary; fluid-structure interaction; computational fluid dynamics;

I. INTRODUCTION

Biological fluid transport is not only dependent upon the method of movement, but also the fluid's physical properties and the size and velocity of the organ or organism. While one mechanism for transport may work well at the macroscale,

Copyright: © 2017 Samson et al. This article is distributed under the terms of the Creative Commons Attribution License (CC BY 4.0), which permits unrestricted use, distribution, and reproduction in any medium, provided the original author and source are credited.

Citation: Julia E. Samson, Nicholas A. Battista, Shilpa Khatri, Laura A. Miller, Pulsing corals: A story of scale and mixing, *Biomath* 6 (2017), 1712169, <http://dx.doi.org/10.11145/j.biomath.2017.12.169>

that same mechanism may not work well at the mesoscale or microscale. For example, reciprocal motion of a fish's caudal fin may not produce adequate forward propulsion if the fish is put into a considerably more viscous fluid than water. If the viscosity is high enough, the fish might not swim at all as no reciprocal fin stroke will yield any net transport of fluid. The fact that reciprocal motions do not generate net movement at small scales is famously known as the Scallop Theorem [1]. The Reynolds number, Re_f , is a dimensionless quantity that describes the ratio of inertial to viscous forces in a fluid and is used to compare fluid transport across scales. For a fluid of density ρ , dynamic viscosity μ , and some characteristic length and frequency scale L and f , respectively, a frequency-based Re_f may be defined as

$$Re_f = \frac{\rho L^2 f}{\mu}. \quad (1)$$

For a Newtonian fluid in a large domain and with a sufficiently low Re_f , it is necessary to use non-reciprocal motions to produce the net transport of fluid. One common example of a non-reciprocal motion is the use of a rotating flagellum like in many bacteria and sperm cells [2], [3]. Beyond locomotion, there are many other applications of fluid transport within biological systems such as the generation of feeding currents [4], the generation of flow for oxygen and nutrient transport [5], the internal pumping of fluids (e.g. the cardiovascular system) [6], flows generated for filtering [7], and flows for photosynthetic enhancement [8]. As is the case for locomotion, different pumping and feeding mechanisms may only be effective over some range of Re_f [9], [10].

In this paper, we quantify the flows produced by a variety of soft corals, including the genera *Xenia* and *Heteroxenia*, that actively pulse and contribute substantially to local ocean mixing, enhancing nutrient availability in reefs. Each individual polyp is made up of eight feather-like tentacles (see Figure 1) positioned at the end of an approximately 5 cm long stalk [11]. These soft corals form colonies up to 60 cm across [11], and polyps within a colony do not normally pulse in synchrony but



Fig. 1: Xeniid coral colonies at the Underwater Observatory, Eilat, Israel.

out of phase [12]. The pulsing motion is generated by active contraction of the muscles in the tentacles, and the expansion of the tentacles is due to passive elastic recoil. Although this behaviour is reminiscent of feeding and prey capture behaviours in other phyla like molluscs or bryozoans, past research has shown that the pulsing is linked to the removal of oxygen from the tissues [12]. This is achieved through increased mixing around the polyps and by allowing oxygen-rich water to be advected away faster than when the corals are not pulsing. Accelerating the removal of oxygen allows for the coral's symbionts to increase their photosynthetic rates, thus increasing the organism's metabolic rate.

On average, the polyp pulsing frequency is about 0.5-1 Hz, and the frequency-based Reynolds number of an individual polyp ranges from about 8 to 36 (see Section II). These corals operate at

an Re_f that is much lower than most other pulsing cnidarians, including jellyfish. In particular, the pulsing soft corals operate in a much lower Re_f regime than the only other benthic cnidarian known to actively pulse to generate exchange currents, the upside-down jellyfish *Cassiopea* spp. Upside-down jellyfish host zooxanthellae in their tissues and, like corals, also benefit from their photosynthetic symbionts [13], [14]. Unlike soft corals that generate exchange currents with their tentacles, upside-down jellyfish create flow by actively contracting and relaxing their gelatinous bell. The biologically relevant Re_f for upside-down jellyfish pulsing in the benthic layer ranges from about 100 to approximately 450 (adult) [15]. As such they operate completely within the inertial range ($Re_f \gg 1$) where reciprocal motions are effective. Several experimental and computational investigations have described the fluid dynamics of upside-down jellyfish [4], [16], [17].

In this paper, we quantify the fluid dynamics of one pulsing polyp over a range of Re_f , both above and below the biologically relevant range. This fully coupled fluid-structure interaction problem is solved using the 3D immersed boundary method. We find that within the biologically relevant range, individual polyps generate a continuous upward jet using a reciprocal motion of the tentacles. This drives new fluid between the tentacles during each pulse and minimizes resampling of the same fluid volume. A slow mixing region is produced during tentacle expansion that is separated from the upward jet, which would provide sufficient time for the uptake of nutrients from the fluid and removal of waste from the tissues. Upon the next contraction, this volume of fluid is expelled and a new volume of fluid is driven between the tentacles upon the subsequent expansion. The continuous upward jet, formation of a slow mixing region during expansion, and continual flow of new fluid toward the polyp in the radial direction are not evident at $Re < 5$ when the flow becomes nearly reversible. For $Re > 40$, the magnitude of flow between the tentacles and the average vertical velocity of the upward jet is reduced.

II. METHODS

A. Coral Motion and Geometry

In this study, we use the frequency-based Reynolds number, Re_f , to describe the flows produced by the coral. The characteristic length, L_T , is set to the tentacle length and the characteristic frequency, f_{coral} , is set to the pulsation frequency. The fluid density and dynamic viscosity are set to that of sea water (see Table I).

To determine the biologically relevant range of Re_f , videos were taken of three coral colonies in the Red Sea off the coast of Eilat, Israel, and of three colonies of cultured corals in the lab. In each video, five individual polyps were tracked to determine the pulse period averaged over 20 cycles. Measurements were also taken from one tentacle on each polyp to determine the length of the tentacle. The pulsing frequency is given as a function of tentacle length in Figure 2. There was no significant correlation between pulsing frequency and size of the coral. The average Re_f was 19.64 ± 7.28 with a minimum of 8.74 and a maximum of 36.0. The average tentacle length was $(6.13 \pm 0.10) \times 10^{-3}$ m and the average pulsing frequency was 0.53 ± 0.043 Hz. For the numerical simulations performed here, we set the frequency and tentacle length to that of a typical coral where $f_{coral} = 1/1.9 \text{ s}^{-1}$ and $L_T = 0.0045$ m. The dynamic viscosity was varied in the simulations to study a range of Re_f , above and below that typical of soft corals. The range of Re_f studied here is 0.5, 1, 5, 10, 20, 40, and 80.

The pulsing motion of the coral was based on kinematics of five live polyps and is detailed elsewhere [18]. To summarize, the motion of the tentacles was quantified by tracking positions along a single tentacle for five pulses. Each polyp was filmed using a single Photron SA3 120K camera at either 125 or 60 frames per second in a quiescent fluid, focusing on the motion of a single tentacle that moved within the plane of focus. In each frame six approximately equispaced points were tracked along the tentacle using DLTdv5 [19]. These positions were then fit with third order polynomials. An averaged motion was constructed

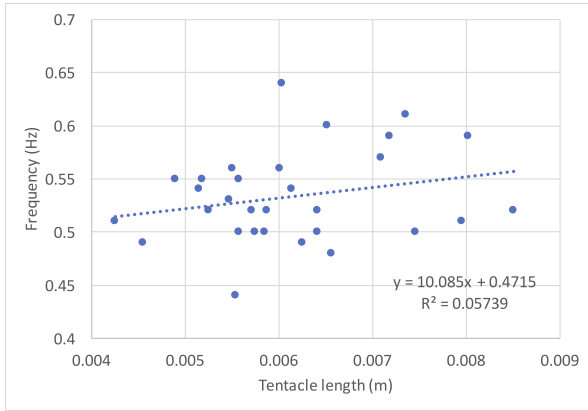


Fig. 2: Pulsing frequency vs. tentacle length for 15 corals in the field (Red Sea, Eilat, Israel) and 15 cultured corals in the lab. There is not a significant relationship between pulsing frequency and size.

Parameter	Variable	Units	Value
Domain Size	D	m	0.06
Spatial Grid Size	dx	m	$D/1024$
Lagrangian Grid Size	ds	m	$D/2048$
Time Step Size	dt	s	1.22×10^{-4}
Total Simulation Time	T	pulses	10
Fluid Density	ρ	kg/m^3	1000
Fluid Dynamic Viscosity	μ	$kg/(ms)$	varied
Tentacle Length	L_T	m	0.0045
Pulsing Period	P	s	1.9
Target Point Stiffness	k_{target}	$kg \cdot m/s^2$	9.0×10^{-9}

TABLE I: Numerical parameters used in the three-dimensional simulations.

by averaging the motion over the five pulses and across five polyps. The averaged motion of the tentacle was used to describe the preferred position of the immersed boundary by tethering the immersed boundary describing the tentacles to time varying target points.

The overall numerical model of the coral consisted of eight tentacles, a base, and no stem. This numerical polyp was placed in the bottom center of the computational domain (see Figure 4). Note

that the presence of the stem does not significantly alter the flow and was neglected. The base of the tentacles was positioned 0.005 m above the bottom of the domain, approximating the length of the stem of the single polyp. The distance from the center of the polyp to the tip of its tentacles at full expansion was approximately 0.0045 m. The distance from the base of the polyp to the tip of the tentacles at full contraction was 0.0037 m. The length of the tentacle was determined by averaging the length measured in each frame for each polyp and then averaging over all five polyps.

The shape of each tentacle was approximated as an isosceles trapezoid with a basal width of 0.00108 m, the average width across all measured polyp tentacles. This average was found by measuring the width of the tentacle base in one frame from each video when a tentacle was parallel to the plane of focus. This distance was then used to construct the numerical tentacle. The width of the top of the tentacle was set to be one fifth of the basal width to circumvent any possible tentacle overlap when the simulated polyp is fully contracted. The average diameter of the polyp’s base was measured by finding the distance between the bottom of two oppositely arranged tentacles in each frame and then averaging across all frames and all videos. This resulted in an average base diameter of 0.00106 m.

A pulsing cycle was divided into three phases as described below (see also Figure 3).

1. The coral begins with all its tentacles in an open, relaxed state. The tentacles then actively contract and the polyp closes. This takes about 28% of the pulse cycle.
2. From the contracted state, the tentacles relax back to their original expanded, resting state. The expansion phase takes about 43% of the pulse cycle.
3. The tentacles remain open and at rest for about 29% of the pulse cycle.

This process then repeats itself.

B. Numerical Method

The immersed boundary method (IB) [20] was used to solve the fully coupled fluid-structure

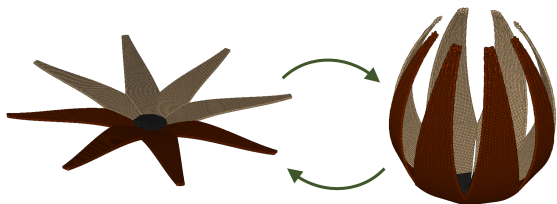


Fig. 3: A single polyp's pulsation cycle. The coral moves from its relaxed state to an actively contracted state and then relaxes back to its original, open, resting state. The two tentacle colors were chosen to differentiate the tentacles in the foreground and background.

interaction problem of a pulsing soft coral in an incompressible, viscous fluid. The IB method has been successfully applied to a variety of problems in biological fluid dynamics with an intermediate Re_f regime, i.e. $0.01 < Re_f < 1000$, including heart development [21], [22], insect flight [23], swimming [24], [25], and dating and relationships [26]. A fully parallelized implementation of the IB method with adaptive mesh refinement, IBAMR [27], was used for the simulations described here. More details on the IB method and IBAMR are found in the Appendix A.

All parameter values used in the computational model are given in Table I. A depiction of the computational domain is given in Figure 4. Note that periodic boundaries are used in the x and z directions, and no-slip conditions are used in the y -direction, corresponding to a solid boundary on the top and bottom of the domain ($\mathbf{u} = 0$ at $y = -0.15$ and $y = 0.45$). The initial conditions of the fluid are set to zero and there is no ambient flow considered. For a study including ambient flow see [28].

C. Lagrangian Coherent Structures

We computed the finite-time Lyapunov exponent (FTLE) to determine Lagrangian coherent structures (LCSs) [29], [30] using Visit 2.12.3 [31]. Within flow fields, LCSs can reveal particle transport patterns that are of potential biological importance, such as in particle capture, predator-prey interactions [32], [33], and locomotion [34].

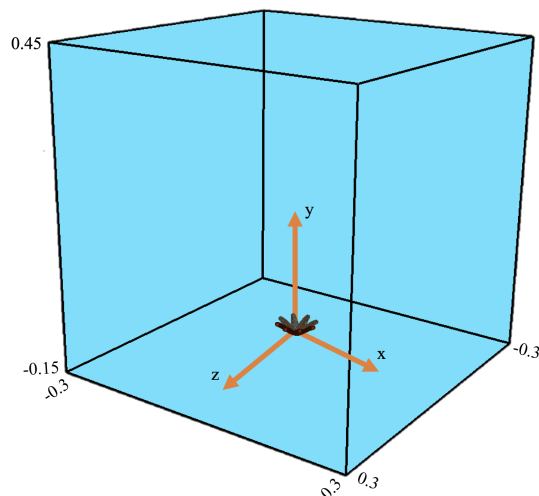


Fig. 4: The computational domain for a single coral polyp. Note that the boundaries in the x - and z -directions are periodic. The boundary conditions in the y -direction are no slip ($\mathbf{u} = 0$ at $y = -0.15$ and $y = 0.45$).

In essence, LCSs provide a method to untangle the overall dynamics of the system in a simplified framework. Trajectories were computed using an instantaneous snapshot of the 3D vector field, and the FTLEs were computed on a regular 128^3 grid using a forward Dormand-Prince (Runge-Kutta) integrator with a relative tolerance of 0.001, an absolute tolerance of 0.0001, a maximum advection time of 0.1s, and a maximum number of steps of 1000.

III. RESULTS

Figures 5-7 show snapshots of the velocity and vorticity generated during the fourth pulsation cycle for three different numerical simulations corresponding to $Re_f = 0.5$, 10, and 80. The velocity vectors point in the direction of flow, the length of the vectors correspond to the magnitude of the flow, and the colormap corresponds to the value of the vorticity taken in the z -direction (out of plane). Both vorticity and fluid velocity were taken on a 2D plane passing through the central axis of the polyp. The tentacles are shown in pink in 3D. The snapshots taken correspond to 5%,

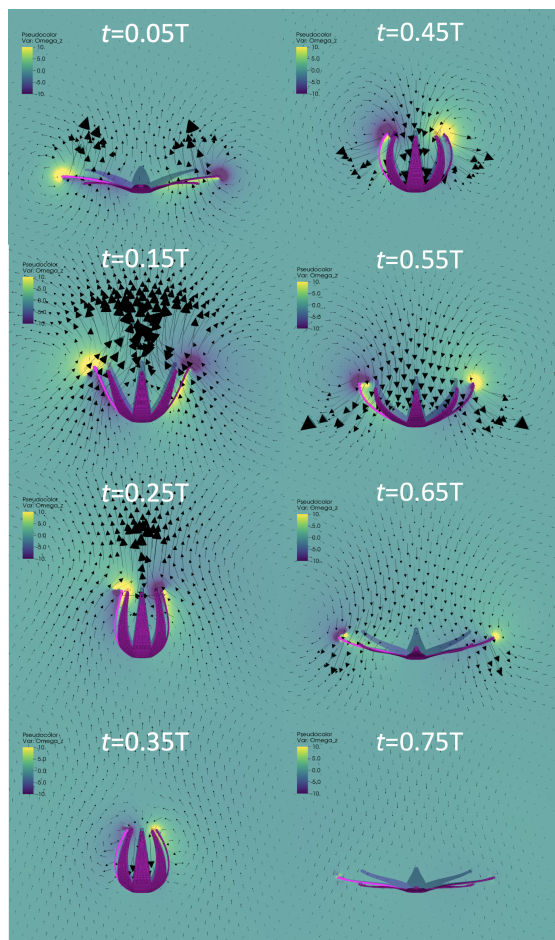


Fig. 5: The z -component of vorticity and the velocity vector field taken on a 2D plane through the central axis of the coral at $Re_f = 0.5$. This Re_f corresponds to a smaller scale than would be observed in nature. The colormap shows the value of ω_z , the arrows point in the direction of flow, and the length of the vectors correspond to the magnitude of the flow. Snapshots are taken during the fourth pulse at times that are 5%, 15%, 25%, 35%, 45%, 55%, 65%, and 75% through the cycle.

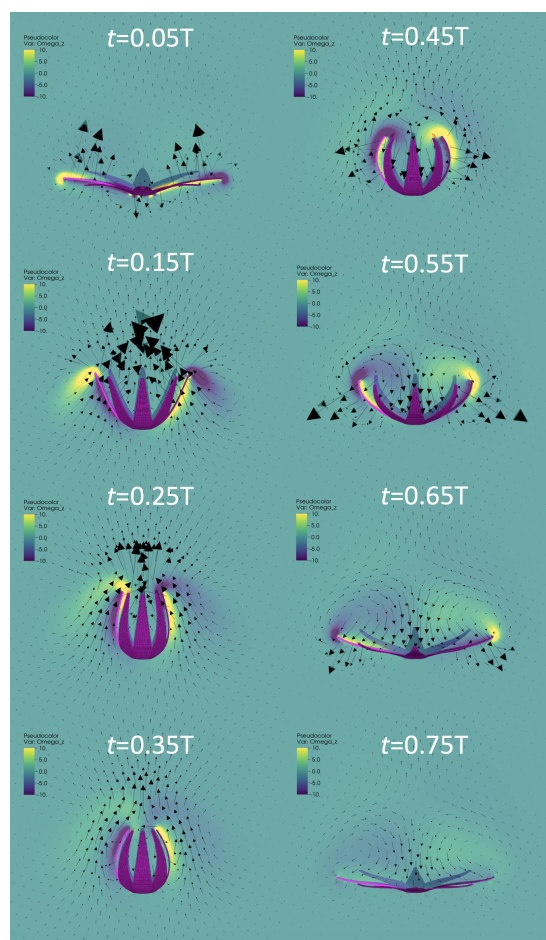


Fig. 6: The z -component of vorticity and the velocity vector field taken on a 2D plane through the central axis of the coral at $Re_f = 10$. This Re_f corresponds to a typical coral polyp. The colormap shows the value of ω_z , the arrows point in the direction of flow, and the length of the vectors correspond to the magnitude of the flow. Snapshots are taken during the fourth pulse at times that are 5%, 15%, 25%, 35%, 45%, 55%, 65%, and 75% through the cycle.

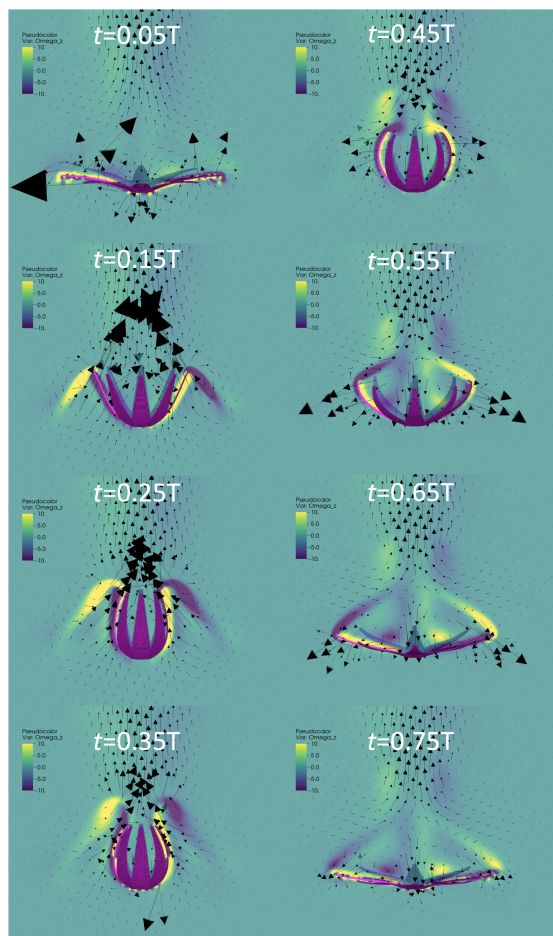


Fig. 7: The z -component of vorticity and the velocity vector field taken on a 2D plane through the central axis of the coral at $Re_f = 80$. This Re_f corresponds to a very large, fast pulsing coral polyp. The colormap shows the value of ω_z , the arrows point in the direction of flow, and the length of the vectors correspond to the magnitude of the flow. Snapshots are taken during the fourth pulse at times that are 5%, 15%, 25%, 35%, 45%, 55%, 65%, and 75% through the cycle.

15%, 25%, 35%, 45%, 55%, 65%, and 75% of the pulsing cycle such that the first three frames show the contraction phase, the next four frames show the expansion phase, and the last frame shows the polyp at rest.

During contraction, regardless of Re_f , there is a clear upwards jet. In addition, vorticity is generated at the tips of the tentacles. At the beginning of expansion ($t = 0.35T$), oppositely spinning vortices are formed at the tips of each tentacle. At higher Re_f , particularly $Re_f = 80$, the vortices formed during contraction separate from the tentacle tips and are advected upwards. The motion of these vortices helps to maintain a strong upward jet above the polyp. At the lower Re_f , (e.g. $Re_f = 0.5$), these vortices quickly dissipate. The direction of flow above the coral also reversed such that fluid is pulled downward between the tentacles. For $Re_f < 1$, the flow is nearly reversible, that is, any fluid pushed away from the polyp during contraction is pulled back during expansion. At intermediate Re_f (e.g. $Re_f = 10$), an upward jet is observed above the polyp during expansion, and fluid below this jet mixes between the tentacles.

During the resting phase (last frame), the fluid comes to rest in the lower Re_f cases. Although the strength of the upwards jet in the $Re_f = 80$ case is greatest, the magnitude of the flow between the tentacles produced by vortices generated during expansion are greater in the $Re_f = 0.5$ and 10 cases. We find strong mixing between the tentacles for $Re_f \leq 30$; this mixing decreases for $Re_f > 30$. This indicates that, near the biologically relevant Re_f , the morphology and motion of the tentacles allow for greater mixing close to the polyp itself.

To compare the relative strength of the upward jets generated by coral polyps across scales, we averaged the y -component of the velocity (in the vertical direction) within a box that was drawn from the tips of the tentacles during full contraction to one tentacle length above that point ($-0.0063m < Y < -0.0018m$). The width of the box was set equal to the diameter of the fully

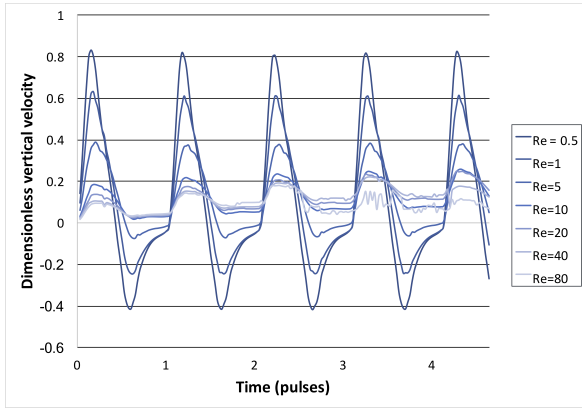


Fig. 8: The spatially averaged dimensionless vertical flow upwards over the polyp (u_y) versus time for five pulse cycles. $Re_f = 0.5, 1, 5, 10, 20, 40,$ and 80 are shown. Flow velocity is nondimensionalized using the tentacle length and pulse duration.

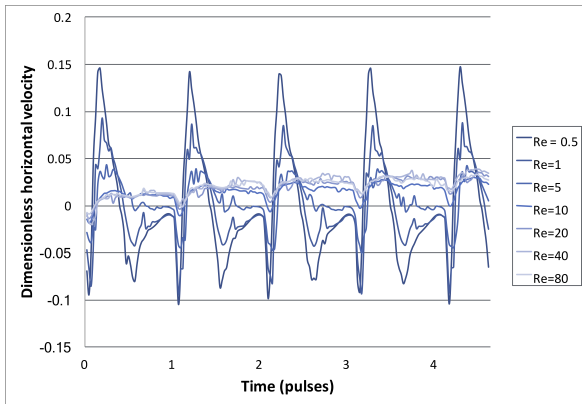


Fig. 9: The spatially averaged dimensionless horizontal flow towards the polyp (u_x) over time during five pulse cycles. $Re_f = 0.5, 1, 5, 10, 20, 40,$ and 80 are shown. Velocity is given as tentacle lengths per pulse.

expanded polyp ($-0.0045m < X, Z < 0.0045m$). The average vertical velocity versus time for five pulses is shown in Figure 8 for $Re_f = 0.5, 1, 5, 10, 20, 40,$ and 80 . Note that the velocities are nondimensionalized by the tentacle length and pulse duration such that $U' = U / \frac{L_T}{P} = U / \frac{0.0045}{1.9}$.

Each Re_f investigated showed a peak average velocity in the upward jet that corresponds to the

end of the contraction phase. Moreover, the largest maximal peak in average velocity corresponds to the lowest $Re_f = 0.5$ case, while the lowest peak corresponds to the highest case, $Re_f = 80$. This is partially due to the fact that we average over a relatively large box. Additionally, the region of motion is larger at lower Re_f due to the relatively large boundary layers (recall that Re_f is lowered by increasing only dynamic viscosity). Immediately following contraction, as the polyp begins to expand, the average velocity drops for each Re_f . In the cases for $Re_f < 5$ there is significant backflow, where the average velocity becomes negative, reaches a minimum, and then slowly approaches zero. Around $Re_f \geq 10$ the average vertical flow decreases during tentacle expansion; however, the net average flow remains upwards. This is significant as the continuous upward jet allows new fluid to be brought to the polyp throughout the pulsing cycle.

While the transition to continuous upward flow occurs at $Re_f = 10$, for $10 \leq Re_f \leq 30$, we have also seen that the tentacle morphology allows for greater mixing near the polyp itself. This suggests that the polyp may be able to enhance its nutrient uptake or waste removal. Note that since the $Re_f = 80$ case has a continuous upward jet but little mixing near the polyp, wastes as well as nutrients would continuously be expelled away from the polyp, leaving less possibility for nutrient absorption. The opposite occurs for the case of $Re_f < 10$, where there is more mixing near the polyp, but the resulting flows are unable to remove wastes away from the polyp.

To compare the relative strength of the flow towards the polyp, we averaged the x -component of the velocity (in the horizontal direction) within a box that was drawn from the tips of the tentacles during full expansion to one tentacle length to the left of that point ($-0.009m < X < -0.0045m$), and in the z -direction, the box was drawn along the diameter of the polyp fully expanded ($-0.0045m < Z < 0.0045m$). In the vertical direction, the box was drawn from the polyp base to the top of the fully contracted ten-

tacle ($-0.01m < Y < -0.0063m$). The average horizontal dimensionless velocity (tentacle lengths per pulse) versus time for five pulses is given in Figure 9 for $Re_f = 0.5, 1, 5, 10, 20, 40,$ and 80 .

For all cases of Re_f considered as the polyp begins to contract, the average flow is away from the polyp during the first 5% of the pulsation period, with the highest average velocities corresponding to the lowest Re_f , $Re_f = 0.5$. The lowest average velocity corresponds to the highest Re_f , $Re_f = 80$. The initial negative values are due to the whip-like motion of the tentacles at the beginning of contraction. Highest average velocities are seen at the lowest Re_f due to the relatively larger boundary layers. After the initial contraction motion, the average velocities become positive, indicating bulk flow towards the polyp. For all Re_f , the average velocity increases until the contraction phase is over. The highest peak average velocity, again, corresponds to the lowest Re_f , $Re_f = 0.5$; however, for $Re_f \geq 10$, their associated peaks of average velocity are almost equivalent. Moreover, for $Re_f \geq 10$, the average velocity remains towards the polyp and almost constant during the expansion and relaxation phases. At the start of the next contraction phase, the average velocity dips, once again within the first $\sim 5\%$ of the pulsation cycle. In contrast, for $Re_f \leq 5$, once the expansion phase begins, the average velocity decreases. For $Re_f \leq 1$, the average velocity decreases, reaches a minimum, and then approaches zero. In the case of $Re_f = 5$, during expansion, the average velocity monotonically decreases toward zero before the start of the next pulsation cycle.

Figure 10 shows temporally and spatially averaged flows as a function of Re_f . The vertical flow above the coral from Figure 8 is temporally averaged during the fourth pulse and plotted in Figure 10A. Figure 10B illustrates the horizontal flow in Figure 9 temporally averaged over the fourth pulse as a function of the Re_f . Both graphs highlight two flow phenomena that depend on Re_f . As the Re_f is lowered, the tentacles entrain a larger volume of fluid. This in turn leads to larger spatially averaged velocities due to the wider jet. Also as the

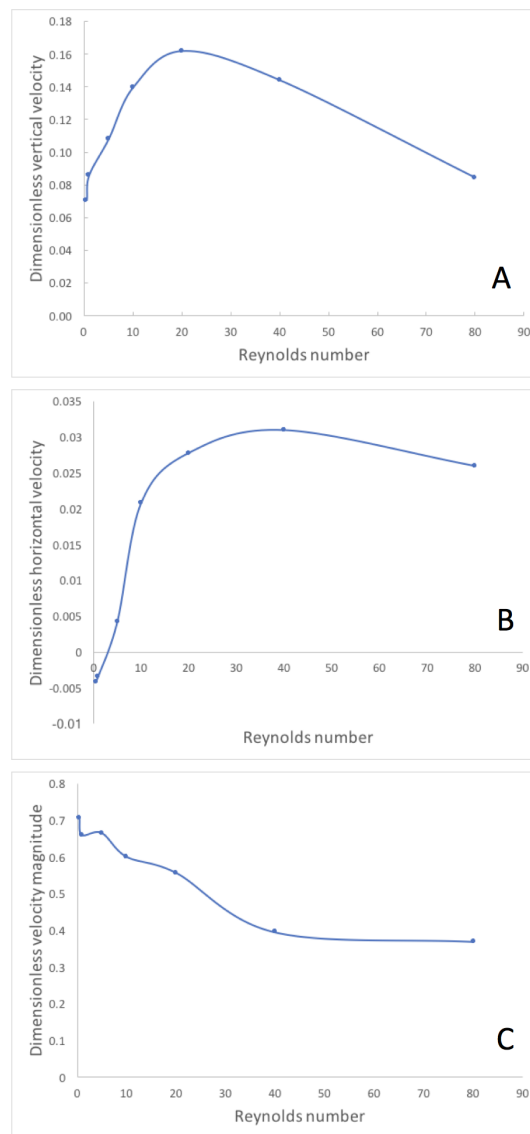


Fig. 10: Temporally and spatially averaged vertical flow above the polyp (A), horizontal flow in the x -direction towards the polyp (B), and velocity magnitude between the tentacles (C) as a function of Re_f . Note that the velocities are nondimensionalized by the tentacle length and pulse duration.

Re_f is decreased, the flow becomes increasingly reversible: the flow moves up and away from the polyp during contraction and back towards the polyp during expansion. Net volumetric flow is maximized for Re_f between about 20 and 30. Reduction in net flow is observed for $Re_f \approx 1$ and lower because the flow becomes reversible. The net flow is reduced as Re_f increases above 30 because the width of the upwards jet decreases.

As a coarse metric of the amount of mixing near the polyp, the magnitude of the velocity of the flow between the tentacles, was spatially and temporally averaged during the last pulse in a volume defined by $-0.001m < X < 0.001m$, $-0.009m < Y < -0.001m$, and $-0.001m < Z < 0.001m$. This averaged flow as a function of Re_f is shown in Figure 10C. The magnitude of flow generally decreases for increasing Re_f , suggesting that more of the fluid is directed into a narrow upward jet as the polyps grow larger. On the other hand, strong flow is generated between the tentacles at Re_f below the biologically relevant range.

A. Lagrangian Coherent Structures

Figure 11 shows contours of the logarithm of the finite-time Lyapunov exponents (FTLE) which illustrate the instantaneous Lagrangian coherent structures (LCS). The contours are shown in a 2D slice through the central axis during the fourth pulsing cycle for $Re_f = 0.5, 20$, and 80 . Note that the LCS were calculated using the entire 3D flow field. Small values of the FTLE highlight regions where flow is attractive, and large values of the FTLE indicate areas in which the flow is repelling [30]. In the case of the polyp, LCSs can be used to highlight regions of fluid that the polyp may sample or that may pass by without interacting with it.

In the biologically relevant case (B) and at higher Re_f (C), we see that fluid is pulled towards the polyp and pushed into the upward jet during the contraction phase ($t = 0.073T$ and $t = 0.17T$). The FTLE values are small between the tentacles during contraction, indicating that this fluid is pushed upward and into the vertical jet

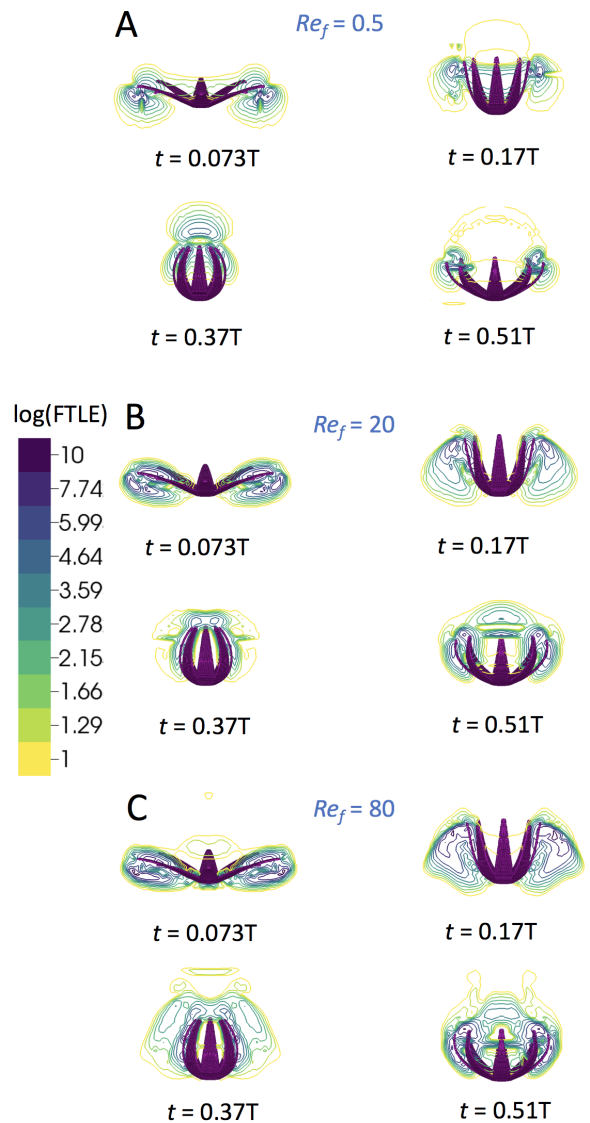


Fig. 11: Contour plot of the finite time Lyapunov exponents (FTLE) illustrating the instantaneous Lagrangian coherent structures during a single polyp's pulsing cycle for (A) $Re_f = 0.5$, (B) $Re_f = 20$ and (C) $Re_f = 80$, using a logarithmic scale.

during this phase. The large FTLE values near the tentacles show that fluid is repelling around the tentacles and the starting vortices. Comparison with the viscous dominated case at $Re_f = 0.5$ (A) shows a region of larger FTLE values between the tentacles. This indicates that the fluid near the bottom of the polyp does not mix as well with the upward jet and is not fully expelled during contraction.

During expansion ($t = 0.37T$ and $t = 0.51T$), large FTLE values directly above the polyp and between the tentacles indicate a region of mixing that is separated from the upward jet in the biologically relevant case ($Re_f = 20$). We also see larger FTLE values in the higher Re_f case (C), but now a more complicated pattern between the tentacles indicating separated mixing regions. For the viscous dominated case (A), the FTLE values are low once the tentacles have partially expanded ($t = 0.51T$). This indicates that the upward jet and the mixing region between the tentacles is no longer separated, and indeed fluid is pulled from above the polyp and into the region between the tentacles. At this Re_f , a new volume of fluid would not be sampled during each pulse.

IV. CONCLUSION

The results of this paper highlight important Re_f transitions in the exchange currents generated by pulsing soft coral. From field measurements, we determined the Re_f of a coral polyp to be 19.64 ± 7.82 with a range of about 8 to 36. In this regime, the flow around the coral polyp is defined by a continuous upward jet, nearly continual radial flow towards the polyp, a slow region of mixing between the tentacles during expansion, and the ejection of the fluid volume into the upward jet during contraction. This pattern implies that a new volume of fluid is brought to the polyp during each polyp cycle that is slow mixed around the tentacles, allowing time for the removal of oxygen from the tissues. Note that the continuous upward jet is significant since, at these scales, the polyp is able to remove waste up and away from the coral colony.

For $Re_f \leq 5$ (below the biologically relevant range), significant backflow is observed during the pulsing cycle. This would result in resampling of the same fluid and reduce waste removal and nutrient exchange. For $Re_f \geq 40$ (above the biologically relevant range), the continuous upward jet becomes narrower, reducing the net transport of fluid away from the coral. The magnitude of flow between the tentacles is also reduced, which could result in less nutrient absorption and exchange.

Spatially and temporally averaged horizontal flow towards the polyp and vertical flow above the polyp show that mass transfer is enhanced across the biologically relevant range of $8 < Re_f < 36$. Spatially and temporally averaged velocity magnitude between the tentacles show that there is less transport near the tentacle base at higher Re_f . Our limited sample of live polyps is insufficient, however to show that an active polyp may not be found at either higher or lower Re_f . Accordingly, it would be interesting to extensively search for the smallest and largest pulsing corals, calculate their effective Re_f , and determine whether or not their pulsing behavior is adapted to push the behavior into more viscous or inertial dominated regimes.

ACKNOWLEDGMENT

The authors would like to thank Uri Shavit and Roi Holzman for introducing us to pulsing soft corals and for their assistance in the field, and the organizers of the 2017 BIOMATH meeting at Kruger Park, South Africa. The authors would also like to acknowledge funding from NSF PHY grant #1505061 (to S.K.) and #1504777 (to L.A.M.), NSF DMS grant #1151478 (to L.A.M.), and NSF DMS grant #1127914 (to the Statistical and Applied Mathematical Sciences Institute). Travel support for J.E.S. was obtained from the Company of Biologists, and J.E.S. was supported by an HHMI International Student Research Fellowship and the Women Diver's Hall of Fame.

APPENDIX

A three-dimensional formulation of the immersed boundary method is discussed here. For

a full review of the immersed boundary method, please see Peskin [20].

A. Governing Equations of IB

The governing equations for an incompressible, viscous fluid motion are given below:

$$\rho \left[\frac{\partial \mathbf{u}}{\partial t}(\mathbf{x}, t) + \mathbf{u}(\mathbf{x}, t) \cdot \nabla \mathbf{u}(\mathbf{x}, t) \right] = \nabla p(\mathbf{x}, t) + \mu \Delta \mathbf{u}(\mathbf{x}, t) + \mathbf{F}(\mathbf{x}, t), \quad (2)$$

$$\nabla \cdot \mathbf{u}(\mathbf{x}, t) = 0, \quad (3)$$

where $\mathbf{u}(\mathbf{x}, t)$ is the fluid velocity, $p(\mathbf{x}, t)$ is the pressure, $\mathbf{F}(\mathbf{x}, t)$ is the force per unit area applied to the fluid by the immersed boundary, ρ and μ are the fluid’s density and dynamic viscosity, respectively. The independent variables are the time t and the position \mathbf{x} . The variables \mathbf{u}, p , and \mathbf{F} are all written in an Eulerian frame on the fixed Cartesian mesh, \mathbf{x} .

The interaction equations, which handle the communication between the Eulerian (fluid) grid and Lagrangian (boundary) grid are written as the following two integral equations:

$$\mathbf{F}(\mathbf{x}, t) = \int \mathbf{f}(s, t) \delta(\mathbf{x} - \mathbf{X}(s, t)) dq \quad (4)$$

$$\mathbf{U}(\mathbf{X}(s, t)) = \int \mathbf{u}(\mathbf{x}, t) \delta(\mathbf{x} - \mathbf{X}(s, t)) d\mathbf{x} \quad (5)$$

where $\mathbf{f}(s, t)$ is the force per unit length applied by the boundary to the fluid as a function of Lagrangian position, s , and time, t , $\delta(\mathbf{x})$ is a three-dimensional delta function, and $\mathbf{X}(s, t)$ gives the Cartesian coordinates at time t of the material point labeled by the Lagrangian parameter, s . The Lagrangian forcing term, $\mathbf{f}(s, t)$, gives the deformation forces along the boundary at the Lagrangian parameter, s . Equation (4) applies this force from the immersed boundary to the fluid through the external forcing term in Equation (2). Equation (5) moves the boundary at the local fluid velocity. This enforces the no-slip condition. Each integral transformation uses a three-dimensional Dirac delta function kernel, δ , to convert Lagrangian variables to Eulerian variables and vice versa.

The way deformation forces are computed, e.g., the forcing term, $\mathbf{f}(s, t)$, in the integrand of Equation (4), is specific to the application. To prescribe the motion of the coral boundary, the boundary points are tethered to target points, which can be moved in a prescribed fashion. The prescribed motion of the boundary itself comes through a penalty term, tethering the Lagrangian points to the target points. The equation describing this model is

$$\mathbf{f}(s, t) = k_{targ} (\mathbf{Y}(s, t) - \mathbf{X}(s, t)), \quad (6)$$

where k_{targ} is a stiffness coefficient and $\mathbf{Y}(s, t)$ is the prescribed position of the target boundary. Note that $\mathbf{Y}(s, t)$ is a function of both the Lagrangian parameter, s , and time, t . Details on other forcing terms can be found in [26], [35].

The delta functions in these Eqs.(4-5) are the heart of the IB. In approximating these integral transformations, the following discretized and regularized delta functions, $\delta_h(\mathbf{x})$ [20], are used,

$$\delta_h(\mathbf{x}) = \frac{1}{h^3} \phi\left(\frac{x}{h}\right) \phi\left(\frac{y}{h}\right) \phi\left(\frac{z}{h}\right), \quad (7)$$

where $\phi(r)$ is defined as

$$\phi(r) = \begin{cases} \frac{1}{8}(3-2|r|+\sqrt{1+4|r|-4r^2}), & 0 \leq |r| < 1, \\ \frac{1}{8}(5-2|r|+\sqrt{-7+12|r|-4r^2}), & 1 \leq |r| < 2, \\ 0, & 2 \leq |r|. \end{cases}$$

B. Numerical Algorithm

As stated in the main text, we impose periodic and no slip boundary conditions on the rectangular domain. To solve Equations (2), (3),(4) and (5) we need to update the velocity, pressure, position of the boundary, and force acting on the boundary at time $n + 1$ using data from time n . The IB does this in the following steps [20], with an additional step (4b) for IBAMR [36], [27]:

Step 1: Find the force density, \mathbf{F}^n on the immersed boundary, from the current boundary configuration, \mathbf{X}^n .

Step 2: Use Equation (4) to spread this boundary force from the Lagrangian boundary mesh to the Eulerian fluid lattice points.

Step 3: Solve the Navier-Stokes equations, Equations (2) and (3), on the Eulerian grid. Upon

doing so, we are updating \mathbf{u}^{n+1} and p^{n+1} from \mathbf{u}^n , p^n , and \mathbf{f}^n . Note that a staggered grid projection scheme is used to perform this update.

Step 4: (4a) Update the material positions, \mathbf{X}^{n+1} , using the local fluid velocities, \mathbf{U}^{n+1} , computed from \mathbf{u}^{n+1} and Equation (5). (4b) If on a selected time-step for adaptive mesh refinement, refine the Eulerian grid in areas of the domain that contain the immersed structure or where the vorticity exceeds a predetermined threshold, .

We note that Step 4b is from the IBAMR implementation of IB. IBAMR is an IB framework written in C++ that provides discretization and solver infrastructure for partial differential equations on block-structured locally refined Eulerian grids [37], [38] and on Lagrangian meshes. Adaptive mesh refinement (AMR) achieves higher accuracy between the Lagrangian and Eulerian mesh by increasing grid resolution in areas of the domain where the vorticity exceeds a certain threshold and in areas of the domain that contain an immersed boundary. AMR improves the computational efficiency by decreasing grid resolution in areas that do not necessitate high resolution.

The Eulerian grid was locally refined near both the immersed boundaries and regions of vorticity where $|\omega| > 0.50$. This Cartesian grid was structured as a hierarchy of four nested grid levels where the finest resolved grid was assigned a resolution of $dx = D/1024$, see Table I. A 1:4 spatial step size ratio was used between each successive grid refinements. The Lagrangian spatial step resolution was chosen to be twice the resolution of the finest Eulerian grid, with $ds = D/2048$.

REFERENCES

- [1] E. Purcell, Life at low reynolds number, *Am. J. Phys.* 45 (1977) 3–11.
- [2] R. H. Dillon, L. J. Fauci, X. Yang, Sperm motility and multiciliary beating: An integrative mechanical model, *Computers & Mathematics with Applications* 52(5) (2006) 749–758.
- [3] S. D. Olson, L. J. Fauci, S. S. Suarez, Mathematical modeling of calcium signaling during sperm hyperactivation, *Mol. Hum. Reprod.* 17(8) (2011) 500–510.
- [4] C. Hamlet, L. A. Miller, T. Rodriguez, A. Santhanakrishnan, The fluid dynamics of feeding in the upside-down jellyfish, *The IMA Volumes on Mathematics and its Applications: Natural Locomotion in Fluids and Surfaces* 155 (2012) 35–51.
- [5] G. A. Truskey, F. Yuan, D. F. Katz, *Transport Phenomena in Biological Systems*, 2nd Edition, Pearson Prentice Hall, Upper Saddle River, NJ, 2004.
- [6] C. S. Peskin, D. M. McQueen, Fluid dynamics of the heart and its valves, in: F. R. Adler, M. A. Lewis, J. C. Dalton (Eds.), *Case Studies in Mathematical Modeling: Ecology, Physiology, and Cell Biology*, Prentice-Hall, New Jersey, 1996, Ch. 14, pp. 309–338.
- [7] A. Y. Cheer, M. A. Koehl, Fluid flow through filtering appendages of insects, *Math. Med. and Biol.: A Journal of the IMA* 4(3) (1987) 185–199.
- [8] O. H. Shapiro, V. I. Fernandez, M. Garren, J. S. Guasto, F. P. Debaillon-Vesque, E. Kramarsky-Winter, A. Vardi, R. Stocker, Vortical ciliary flows actively enhance mass transport in reef corals, *PNAS* 111(37) (2014) 13391–13396.
- [9] A. Baird, T. King, L. A. Miller, Numerical study of scaling effects in peristalsis and dynamic suction pumping, *Biol. Fluid Dyn. Model. Comput. Appl.* (2014) 129148.
- [10] R. Holzman, V. China, S. Yaniv, M. Zilka, Hydrodynamic constraints of suction feeding in low reynolds numbers, and the critical period of larval fishes, *Integrative and Comparative Biology* 55 (2015) 4861.
- [11] E. Lieske, R. F. Myers, *Coral Reef Guide: Red Sea*, 2nd Edition, Harper Collins, NY, NY, 2004.
- [12] M. Kremien, U. Shavit, T. Mass, A. Genin, Benefit of pulsation in soft corals, *PNAS* 110(22) (2013) 8978–8983.
- [13] E. H. Kaplan, R. T. Peterson, S. L. Kaplan, *A Field Guide to Southeastern and Caribbean Seashores: Cape Hatteras to the Gulf Coast, Florida, and the Caribbean*, 2nd Edition, Houghton Mifflin Harcourt, Boston, MA, 1988.
- [14] W. K. Fitt, K. Costley, The role of temperature in survival of the polyp stage of the tropical rhizostome jellyfish *Cassiopea xamachana*, *J. Exp. Marine Biol. Ecol.* 222 (1998) 79–91.
- [15] C. Hamlet, Mathematical modeling, immersed boundary simulation, and experimental validation of the fluid flow around the upside-down jellyfish *Cassiopea xamachana*, Ph.D. thesis, University of North Carolina at Chapel Hill, Chapel Hill, NC (2011).
- [16] C. Hamlet, L. A. Miller, Feeding currents of the upside-down jellyfish in the presence of background flow, *Bull. Math. Bio.* 74(11) (2012) 2547–2569.
- [17] C. Hamlet, L. A. Miller, Effects of grouping behavior, pulse timing and organism size on fluidflow around the upside-down jellyfish, *Cassiopea sp.*, *Biological Fluid Dynamics: Modeling, Computation, and Applications*, Contemporary Mathematics, American Mathematical Society 628 (2014) 173–187.
- [18] J. E. Samson, D. Ray, U. Shavit, R. Holzman, L. A. Miller, S. Khatri, Pulsing corals are efficient mesoscale mixers.
- [19] T. L. Hedrick, Software techniques for two- and three-

- dimensional kinematic measurements of biological and biomimetic systems, *Bioinspiration and Biomimetics* 3 (3) (2008) 034001.
- [20] C. S. Peskin, The immersed boundary method, *Acta Numerica* 11 (2002) 479–517.
- [21] N. A. Battista, A. N. Lane, L. A. Miller, On the dynamic suction pumping of blood cells in tubular hearts, in: A. Layton, L. A. Miller (Eds.), *Women in Mathematical Biology: Research Collaboration*, Springer, New York, NY, 2017, Ch. 11, pp. 211–231.
- [22] N. A. Battista, A. N. Lane, J. Liu, L. A. Miller, Fluid dynamics of heart development: Effects of trabeculae and hematocrit, *Math. Med. Biol.* doi:10.1093/imammb/dqx018.
- [23] S. K. Jones, R. Laurenza, T. L. Hedrick, B. E. Griffith, L. A. Miller, Lift- vs. drag-based for vertical force production in the smallest flying insects, *J. Theor. Biol.* 384 (2015) 105–120.
- [24] A. P. Hoover, L. A. Miller, A numerical study of the benefits of driving jellyfish bells at their natural frequency, *J. Theor. Biol.* 374 (2015) 13–25.
- [25] A. P. Hoover, B. E. Griffith, L. A. Miller, Quantifying performance in the medusan mechanospace with an actively swimming three-dimensional jellyfish model, *J. Fluid. Mech.* 813 (2017) 1112–1155.
- [26] N. A. Battista, W. C. Strickland, L. A. Miller, Ib2d: a python and matlab implementation of the immersed boundary method, *Bioinspir. Biomim.* 12(3) (2017) 036003.
- [27] B. E. Griffith, An adaptive and distributed-memory parallel implementation of the immersed boundary (ib) method (2014) [cited October 21, 2014]. URL <https://github.com/IBAMR/IBAMR>
- [28] N. A. Battista, J. E. Samson, S. Khatri, L. A. Miller, Under the sea: Pulsing corals in ambient flow, *Mathematical Methods and Models in Biosciences*, Biomath Forum, Sofia (2017) 22–35 url: <http://www.biomathforum.org/biomath/index.php/texts/article/view/1107>.
- [29] G. Haller, Lagrangian coherent structures from approximate velocity data, *Phys. Fluids* 14 (2002) 1851–1861.
- [30] S. C. Shadden, F. Lekien, J. E. Marsden, Definition and properties of lagrangian coherent structures from finite-time lyapunov exponents in two-dimensional aperiodic flows, *Physica D* 212 (2005) 271.
- [31] H. Childs, E. Brugger, B. Whitlock, J. Meredith, S. Ahern, D. Pugmire, K. Biagas, M. Miller, C. Harrison, G. H. Weber, H. Krishnan, T. Fogal, A. Sanderson, C. Garth, E. W. Bethel, D. Camp, O. Rübél, M. Durant, J. M. Favre, P. Navrátil, *VisIt: An End-User Tool For Visualizing and Analyzing Very Large Data*, in: *High Performance Visualization—Enabling Extreme-Scale Scientific Insight*, 2012, pp. 357–372.
- [32] T. Sapsis, J. Peng, G. Haller, Instabilities on prey dynamics in jellyfish feeding, *Bulletin of Mathematical Biology* 73 (8) (2011) 1841–1856. doi:10.1007/s11538-010-9594-4. URL <https://doi.org/10.1007/s11538-010-9594-4>
- [33] J. Peng, J. O. Dabiri, Transport of inertial particles by lagrangian coherent structures: application to predator-prey interaction in jellyfish feeding, *Journal of Fluid Mechanics* 623 (2009) 75–84.
- [34] M. M. Wilson, J. Peng, J. O. Dabiri, J. D. Eldredge, Lagrangian coherent structures in low reynolds number swimming, *J. Phys.: Condens. Matter* 21 (20) (2009) 204105.
- [35] N. A. Battista, W. C. Strickland, A. Barrett, L. A. Miller, Ib2d reloaded: a more powerful python and matlab implementation of the immersed boundary method, arXiv: <https://arxiv.org/abs/1707.06928>.
- [36] B. E. Griffith, Simulating the blood-muscle-vale mechanics of the heart by an adaptive and parallel version of the immersed boundary method, Ph.D. thesis, Courant Institute of Mathematics, New York University, New York, NY (2005).
- [37] M. J. Berger, J. Olinger, Adaptive mesh refinement for hyperbolic partial-differential equations, *J. Comput. Phys.* 53 (3) (1984) 484–512.
- [38] M. J. Berger, P. Colella, Local adaptive mesh refinement for shock hydrodynamics, *J. Comput. Phys.* 82 (1) (1989) 64–84.

SUPPLEMENTARY MATERIAL LINKED TO THE ONLINE VERSION

1. Movie of velocity and vorticity of flow field around pulsing coral at $Re_f = 0.5$.
2. Movie of velocity and vorticity of flow field around pulsing coral at $Re_f = 10$.
3. Movie of velocity and vorticity of flow field around pulsing coral at $Re_f = 80$.